metals

MDPI

Article

Microstructural Characterization of Surface Softening Behavior for Cu-Bearing Martensitic Steels after Laser Surface Heat Treatment

Eun-Joon Chun [1,*], Ahjin Sim [1,2], Min-Su Kim [3] and Namhyun Kang [2]

[1] Laser Industrial Technology Research Group, Busan Machinery Research Center, Korea Institute of Machinery and Materials (KIMM), 48, Mieumsandan 5-ro 41beon-gil, Gangseo-gu, Busan 46744, Korea; pnuqb@naver.com

[2] Department of Materials Science and Engineering, Pusan National University, 2, Busandaehak-ro 63beon-gil, Geumjeong-gu, Busan 46241, Korea; nhkang@pusan.ac.kr

[3] Joining and Welding Research Institute, Osaka University, 11-1 Mihogaoka, Ibaraki, Osaka 567-0047, Japan; mskim927@gmail.com

* Correspondence: eunjoonchun@kimm.re.kr; Tel.: +82-51-310-8132; Fax: +82-51-310-8199

Received: 12 June 2018; Accepted: 20 June 2018; Published: 20 June 2018

Abstract: The surface hardening and softening behavior of two types of medium carbon martensitic steel (AISI P20-improved and AISI P21) after laser-assisted heat treatment was quantitatively compared. The laser-assisted heat treatment was performed using a high-power diode laser with in situ temperature and laser power control (two-color pyrometer system). For AISI P20-improved steel, the peak hardness value within the hardening zone was approximately 640 HV after laser-assisted heat treatment at a temperature of 1473 K. In other words, the hardness increased by 120% from the base metal level (290 HV). However, for AISI P21 steel, the hardness within the heat-treated zone did not change from that of the base metal (410 HV), despite being accompanied by martensite transformation. Moreover, it was clearly observed that the hardness dropped below the level of the base metal at the boundary between the heat-treated zone and the base metal region, forming a softening zone. This softening behavior was strongly related to coarsening and a looser distribution of Cu precipitates compared with that of the base metal region, despite the same matrix phase (i.e., tempered martensite) existing in the softening zone and in the base metal region.

Keywords: Cu-bearing steel; diode laser; surface heat treatment; softening; Cu precipitate; coarsening

1. Introduction

In recent years, plastics or fiber-reinforced plastics have played an important role in engineering materials. They have been extensively applied to automobiles, shipbuilding, airplanes, and home appliance housings owing to their specific characteristics, such as corrosion resistance, resistance to chemicals, low density, and ease of manufacture [1]. In this regard, plastic materials have increasingly replaced metallic components in these industrial fields. Over 30% of all plastic components in various industries are manufactured by the injection molding process because it can produce complex-shape plastic products and exhibits good dimensional accuracy with a short cycle [2]. Also, the continuous rise in high-strength engineering plastics has led to the necessity to develop superior mold steel to improve durability. For instance, in the automotive industry, many components have been manufactured by the plastic injection of glass-fiber-reinforced plastics. However, this type of reinforced plastic material is extremely abrasive on the mold surface, which is a major problem in the plastic injection industry; the tips scratch and wear the mold surface, making them rough and decreasing the surface brightness of the injected products [2,3]. Failure of the molds is predominantly

caused by surface damage, such as wear, fatigue, and corrosion. To solve this problem, several surface modification processes have been applied to the surface of injection molds, including gas nitriding, plasma nitriding, plasma carburizing, chemical vapor deposition, ion beam treatment, and electron beam processes [4,5].

Among the numerous available manufacturing processes, laser-beam-assisted processes are particularly versatile because of their diverse application range and superior manufacturing efficiency, including welding [6–8], cladding [9], surface alloying [10,11], selective melting [12–14], shock peening [15,16], and riveting [17]. Selective control of surface material properties is also possible through laser processing. A high-power diode laser is often used in this type of surface modification process [18–24] because of its high metal absorptivity and typically rectangular beam shape (similar to a top hat in both directions), which allows for a larger treatment area than CO_2 [25], Nd:YAG [26], disks [27], and fiber lasers [28,29]. Therefore, the diode laser process is a strong candidate for the surface modification treatment of mold material used in the plastic injection process owing to its superior work efficiency compared to gas nitriding, plasma nitriding, plasma carburizing, chemical vapor deposition, ion beam treatment, and electron beam processes. Although many studies have reported surface modification using diode lasers for various metallic materials such as self-fluxing alloys, low-carbon steel sheets, and tool steels, similar studies for plastic mold steels (for instance, AISI P20-improved (KP4M®) and P21 (NAK80), etc.) remain insufficient.

Especially, AISI P21 steel is a well-known, age-hardened, Cu-bearing martensitic steel whose strength is further achieved by precipitation of Cu-rich particles during aging instead of the precipitation of carbide particle. In this regard, several fundamental studies on the effect of Cu precipitation on mechanical properties have been reported [30,31]. Hsiao et al. investigated the age hardening and tempering behavior of AISI P21 steel according to carbides and Cu precipitation and optimized the heat treatment conditions of peak age hardening [30]. They also suggested that coarsening of the precipitates resulted in a significant loss of strength after overaging [30]. Consequently, it is possible that further surface treatment of this type of material, such as laser-assisted heat treatment, would negatively affect the optimized microstructure of the base metal. Yao et al. reported local softening behavior of the surface within the overlapping zone after multipass laser-assisted heat treatment of medium carbon with alloyed steels, which did not involve Cu-bearing steel [32]. Moreover, although Bouquet et al. [33] and Kwok et al. [34] reported the surface heat treatment results of plastic mold steels, relevant fundamental studies on local softening behavior based on microstructural characterization have not been reported for Cu-bearing plastic mold steels, such as AISI P21.

Consequently, this study aims to characterize the local surface softening behavior of AISI P21 steel according to its microstructural evolution during laser-assisted heat treatment. These results were compared with another type of plastic mold steel (AISI P20-improved) hardened by laser-assisted heat treatment. For this study, the authors constructed a surface hardening treatment system consisting of a high-power diode laser with in situ temperature and laser power control.

2. Materials and Experimental Procedures

2.1. Materials

In this study, two types of commercial plastic mold steels (AISI P20-improved and AISI P21) were used, referred to here as P20-improved and P21, respectively. Table 1 lists their chemical compositions.

Table 1. Chemical compositions of materials used in this study (mass%).

Materials	C	Ni	Si	Mn	Cr	Mo	Cu	Fe
AISI P20 improved	0.38	0.12	0.26	1.02	1.72	0.46	-	Bal.
AISI P21	0.15	3.00	0.30	1.60	0.30	0.30	1.03	Bal.

2.2. Experimental Procedures

The laser beam was irradiated at the surface of the plastic mold steel (specimen dimensions: 150 mm × 100 mm × 15 mm) using a diode laser system (4 kW TeraBlade Laser, TeraDiode Inc., Wilmington, MA, USA) with a laser wavelength of 970 nm in continuous wave mode. The laser irradiation conditions are listed in Table 2. Laser beam irradiation was performed using temperature control in real time. The incident laser power was automatically controlled to regulate the hardening treatment temperature of the specimen surface, which was monitored by a two-color pyrometer (LASCON®, Dr. Mergenthaler GmbH, Neu-Ulm, Germany) positioned coaxial to the laser beam. The heat treatment was performed in a temperature range of 1073–1473 K. The laser spot over the substrate was a 24.0 mm × 1.0 mm rectangle. The maximum laser power density was 2.5×10^3 at a heat treatment temperature of 1473 K. The focal length was 310 mm and the focal point of the laser beam was at the specimen surface (defocus distance of 0 mm), with a laser beam scan speed of 5.0 mm/s. Figure 1 depicts the laser-assisted heat treatment system and the specimen arrangement. The qualitative analysis of phase in base metals was performed by X-ray diffraction (XRD, Ultima IV, Rigaku, Japan) with Cu-Kα radiation. The diffraction data were collected over a 2θ range from 40 to 100 degrees (°). The microstructure of the base metals and the heat-treated specimen was observed by optical microscopy (OM, BX51M, Olympus, Tokyo, Japan) and scanning electron microscopy (SEM, SNE-4500M, SEC, Suwon-si, Korea). To characterize the microstructural evolution after heat treatment, two types of transmission electron microscopy (TEM) analysis were performed by employing thin film methods (with JEM-2100F, JEOL, Japan) and replica methods (with JEM-2010, JEOL, Tokyo, Japan). Furthermore, TEM samples from thin film methods were prepared using a multibeam focused ion beam (FIB) and SEM system (JIB-4500, JEOL, Japan). During TEM analysis, energy-dispersive X-ray spectroscopy (EDS, X-Max 65T, Oxford, UK) was also employed to confirm element distributions. To confirm the effect of heat treatment conditions on the mechanical properties of the hardened layer, Vickers hardness analysis (MMT-X7, Matsuzawa, Japan) was performed with a testing load of 0.5 kgf and a dwell time of 10 s.

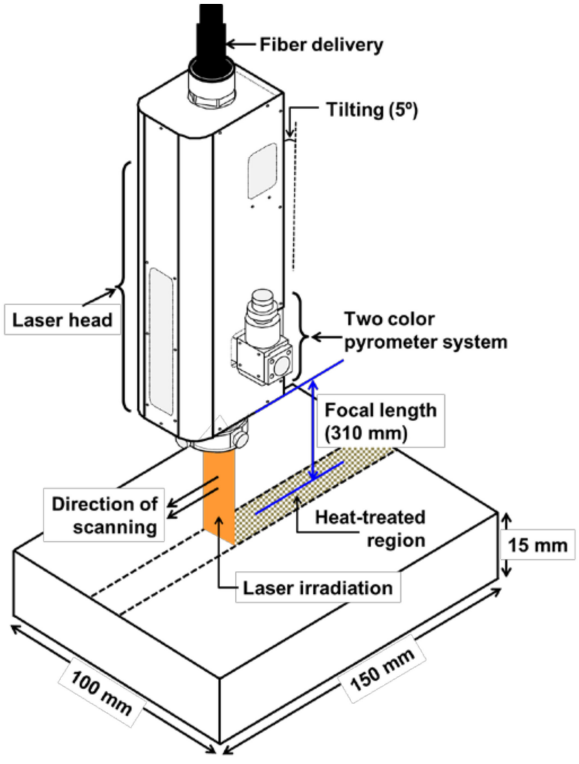

Figure 1. Schematic description of specimen arrangement and laser-assisted heat treatment.

Table 2. Conditions for laser-assisted heat treatment.

Parameters	Values
Oscillator	4 kW direct diode laser
Wavelength of laser beam (nm)	970
Beam dimension (mm)	24 × 1
Maximum laser power density (W/cm^2)	2.5 × 10^3
Direction of beam irradiation	5° tilting from normal direction of specimen
Focal length (mm)	310
Defocus distance (mm)	0
Scan speed of laser beam (mm/s)	5
Temperature of heat treatment (K)	1073–1473

3. Results and Discussion

3.1. Microstructure of Base Metals (As-Recieved)

Figure 2 shows microstructures and Figure 3 also demonstrates results of XRD qualitative analysis for two types of base metal. It has been well known that these two kinds of materials accompany quenching with the age-hardening process [30,31], thus the main constituent phase was surmised as tempered martensite. From Figures 2 and 3, even though morphology of the microstructure slightly differed between P20-improved and P21 steels (displayed in Figure 2), all the peak points obtained from XRD indicated the martensite phase (displayed in Figure 3). Consequently, the matrix phase could be confirmed as tempered martensite for both materials.

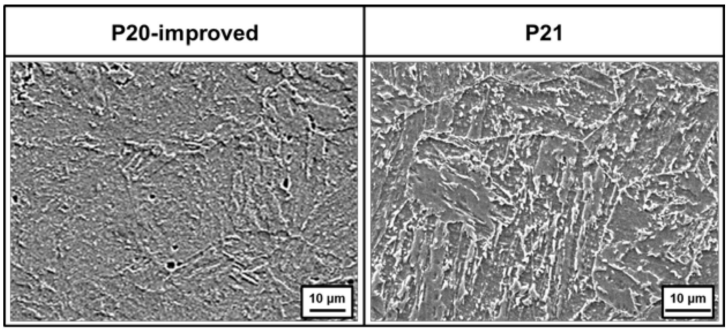

Figure 2. SEM micrographs of P20-improved and P21 steels (as-received).

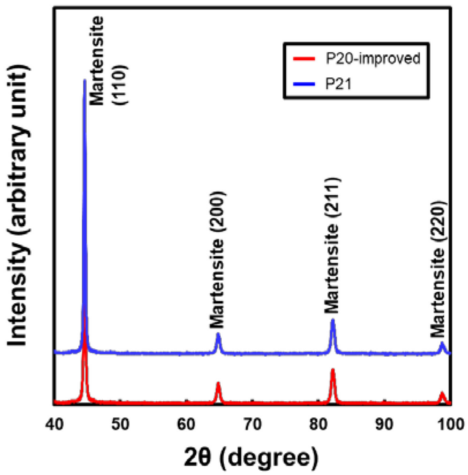

Figure 3. Patterns of XRD obtained from P20-improved and P21 steels (as-received).

3.2. Determining Heat Treatment Conditions from Thermodynamic Calculations

Figure 4 shows the thermodynamic calculation results for the compositions of (a) P20-improved and (b) P21, obtained using Thermo-Calc software system (2018b, TCFE9 database, Thermo-Calc Software, Sweden). The fully austenite (γ) phase region (above the A_3 temperature) begins at 1045 K for P20-improved and 1008 K for P21 steels. For transformation hardening during heat treatment, the temperature set during the laser-assisted heat treatment was above the A_3 temperature, i.e., from 1073 K to 1473 K for both materials.

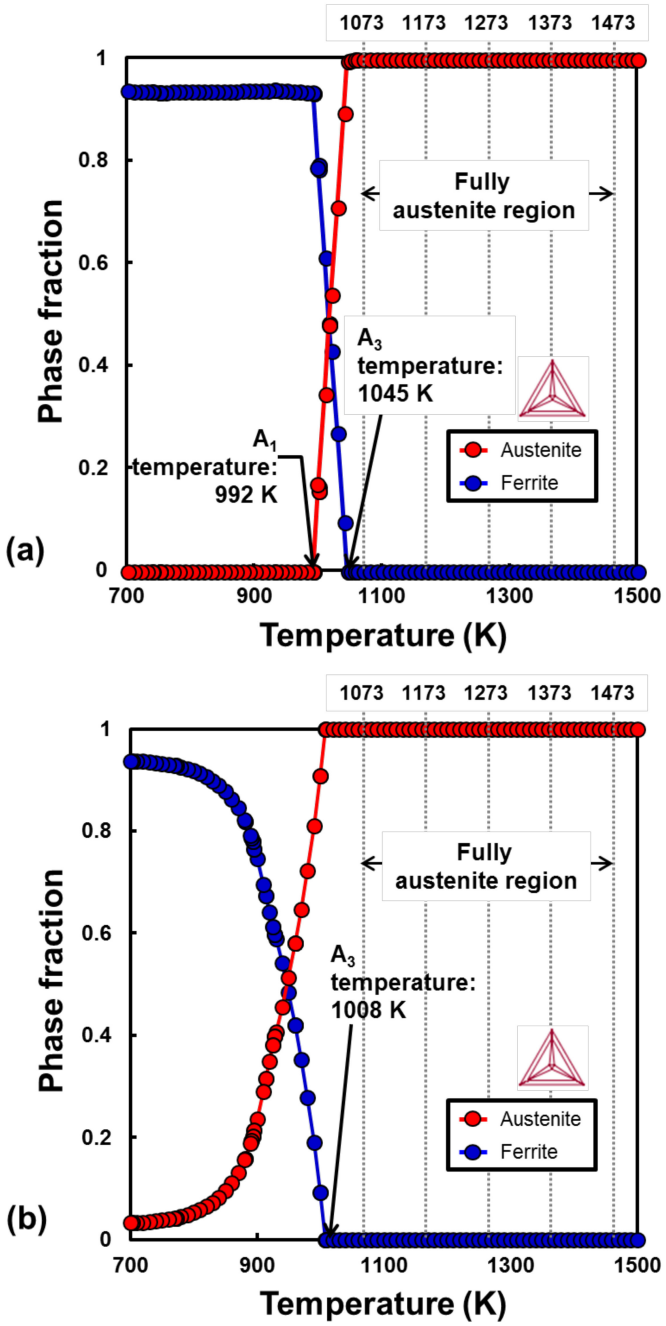

Figure 4. Thermodynamic calculations of phase fraction as a function of temperature for (**a**) P20-improved steel and (**b**) P21 steel.

3.3. Laser Power and Surface Temperature during Laser-Assisted Heat Treatment

Figure 5 shows the typical laser power and temperature history during laser-assisted heat treatment for P20-improved at 1373 K over 25 s. The temperature remained constant while the laser power was controlled over time. The laser power reached approximately 1.9 kW at the beginning of heat treatment, then decreased to a stable value of 1.2 kW. Even though the stable value of laser power also increased or decreased as the set temperature changed, similar trends of the temperature and laser power were confirmed from other heat treatment conditions. Furthermore, these tendencies could be confirmed from P21 steel. In other words, the selected heat treatment temperature described in Section 3.2 was precisely maintained during laser irradiation by automatically controlling the laser power.

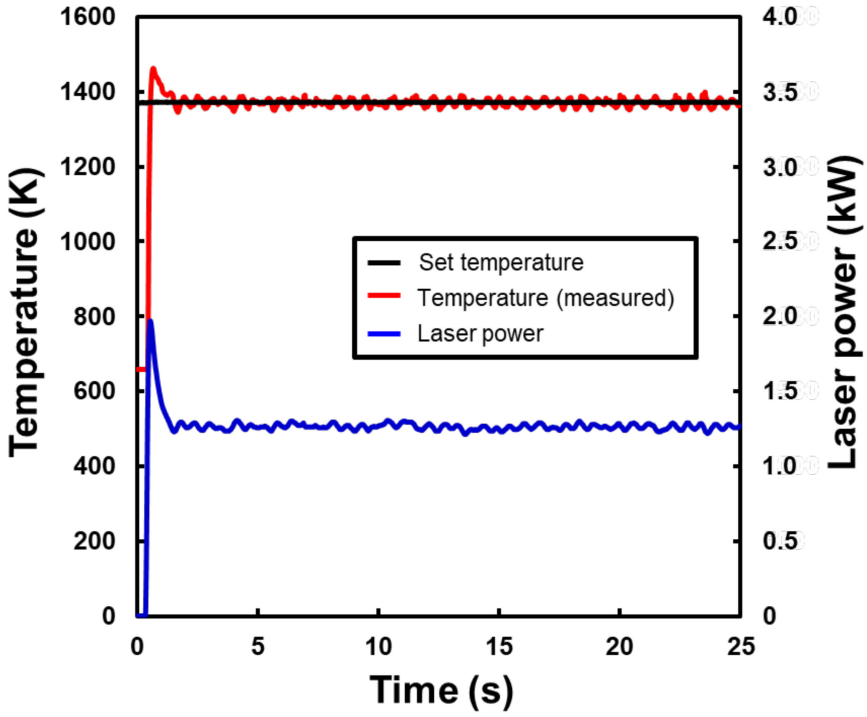

Figure 5. Typical laser power and temperature history during laser-assisted heat treatment at target temperatures of 1373 K for P20-improved steel.

3.4. Cross-Sectional Macrostructure Variations with Temperature

Figure 6 shows the cross-sectional macrostructure for (a) P20-improved and (b) P21 after laser-assisted heat treatment at 1073, 1173, 1273, 1373, and 1473 K. For both materials, the conduction shape of the heat-treated zone (marked by the white square box) was clearly observed with an increase in heat treatment temperature from 1073 K to 1473 K, and the area was also enlarged with an increase in the temperature. Figure 7 summarizes the relationship between the heat treatment temperature and cross-sectional area of the heat-treated zone for both P20-improved and P21. The cross-sectional area increased from 1.9 mm^2 to 12.2 mm^2 for P20-improved. A similar tendency was confirmed for P21. This was attributed to the high laser power while increasing the heat treatment temperature.

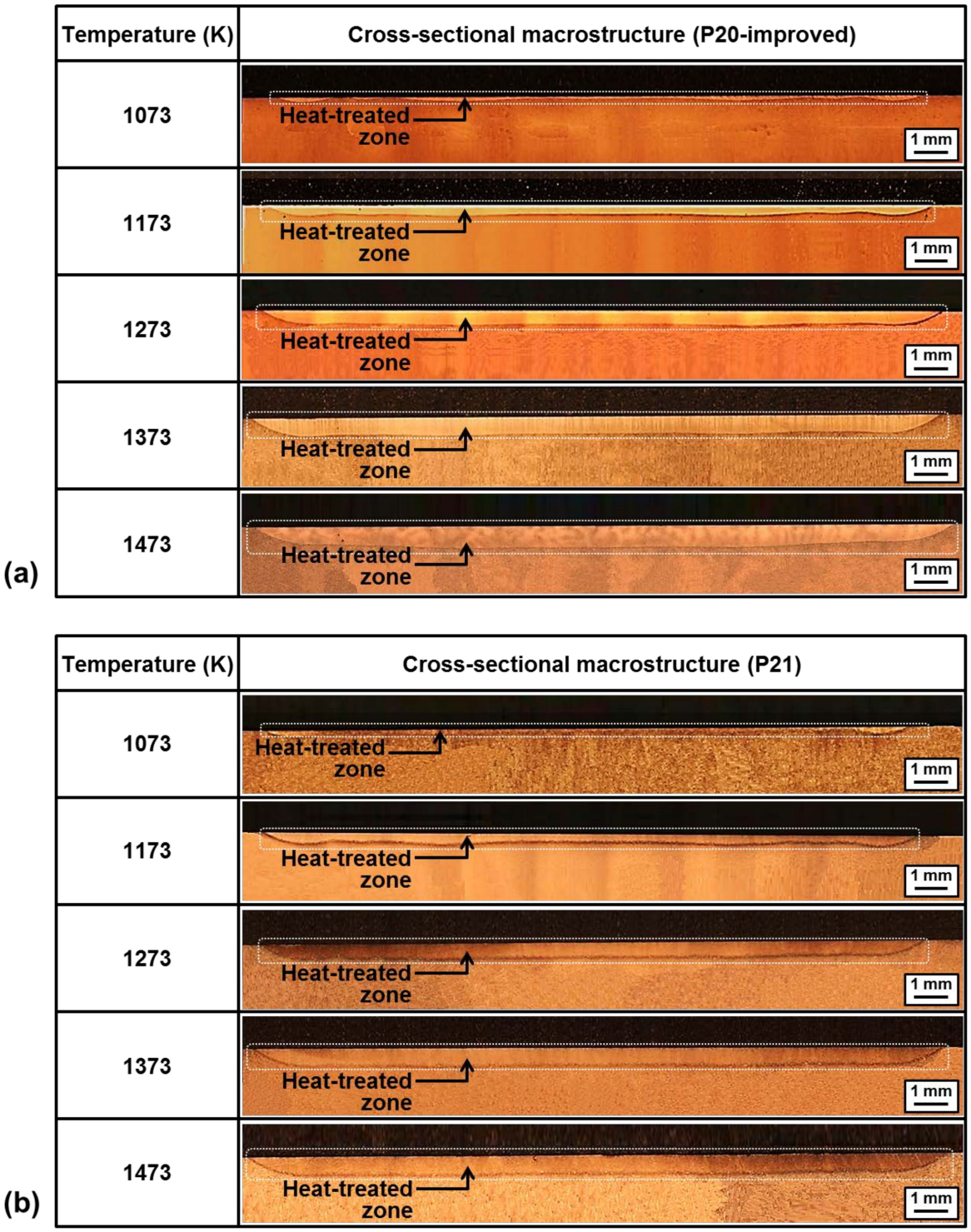

Figure 6. Cross-sectional macrostructure after laser-assisted heat treatment for (**a**) P20-improved steel and (**b**) P21 steel.

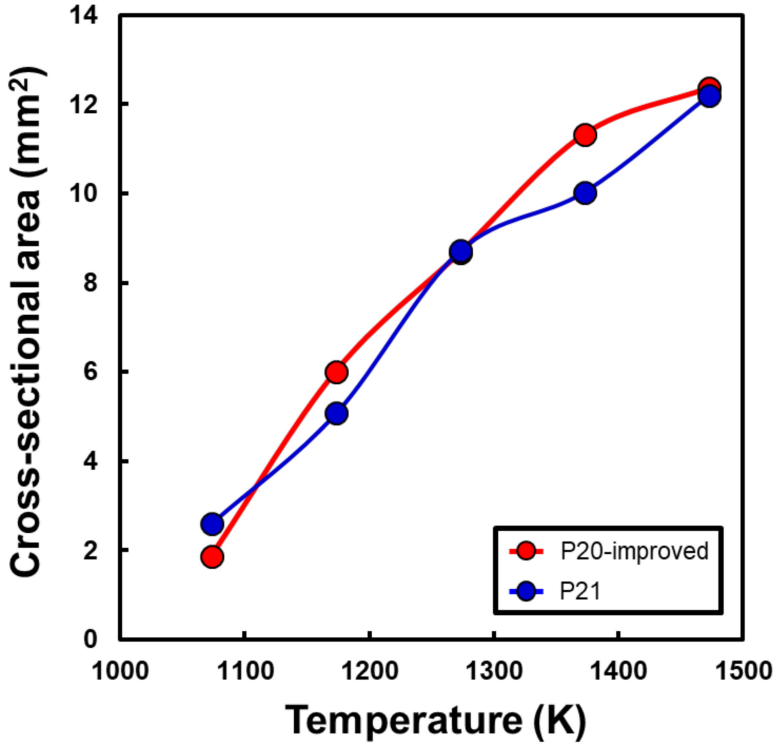

Figure 7. Relationship between the laser-assisted heat treatment temperature and cross-sectional area of the heat-treated zone for P20-improved and P21 steels.

3.5. Hardening and Softening Behavior after Laser-Assisted Heat Treatment

Figure 8 shows the representative hardness distribution with the corresponding cross-sectional macrostructure of P20-improved after heat treatment at 1473 K. The hardness was mapped with four layers from the surface of the specimen. At a heat treatment temperature of 1473 K, the hardness of the heat-treated zone increased from approximately 290 HV (hardness level of the base metal) to 640 HV (maximum hardness). In other words, it was clearly confirmed that 120% of the hardness increase in P20-improved steel from the base metal hardness level was attained after heat treatment using a high-power diode laser. At other temperatures, a similar level of hardness increment could be confirmed.

Figure 9 shows the typical hardness distribution with corresponding cross-sectional macrostructures for P21 after laser-assisted heat treatment at 1473 K. Similar to P20-improved, the hardness was mapped with four layers from the surface. The hardness level of the base metal was approximately 410 HV. However, the hardness within the heat-treated zone (from the first to third layers of hardness mapping) did not change from that of the base metal. Moreover, the hardness clearly dropped below the level of the base metal at the fourth layer (the boundary region between the heat-treated zone and the base metal region) of hardness mapping; i.e., a softening zone appeared. A similar tendency could be confirmed in specimens heat treated at other temperatures. P21 is a well-known, Cu-bearing, age-hardened steel based on martensite as a matrix phase. During aging, tempering of martensite and age hardening occurred simultaneously, resulting in a hardness level from approximately 400 to 450 HV [30]. It has been reported that the hardness of P21 decreased to approximately 300 HV during overaging because of coarsening of Cu-based precipitates [30]. It is thought that the hardness decrease at the fourth layer in Figure 9 is related to the fact that the temperature in the fourth layer during heat treatment was within the overaging temperature range. Further analysis of this softening behavior is performed in Section 3.7.

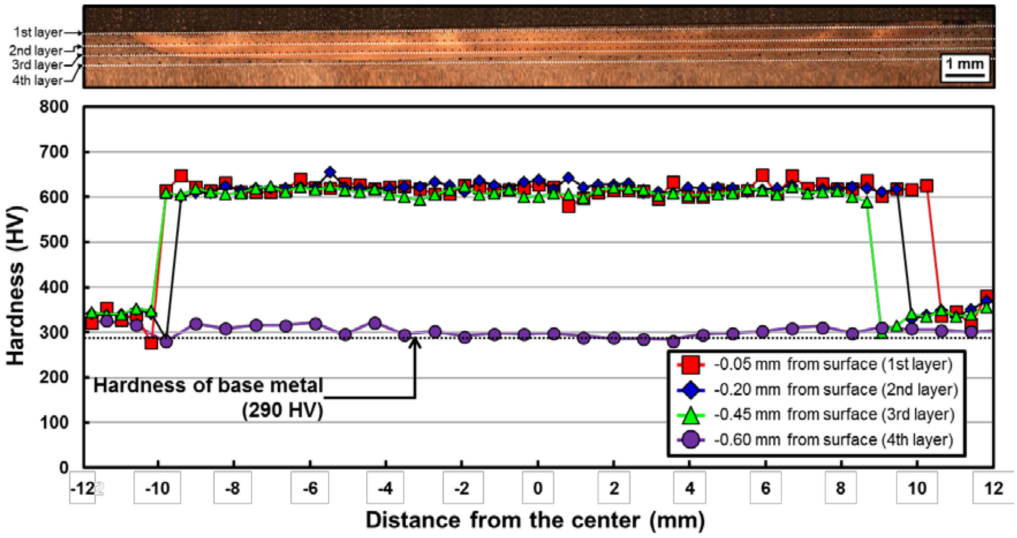

Figure 8. Hardness distribution and corresponding macrostructure of the heat-treated cross-sectional specimen at temperatures of 1473 K for P20-improved steel.

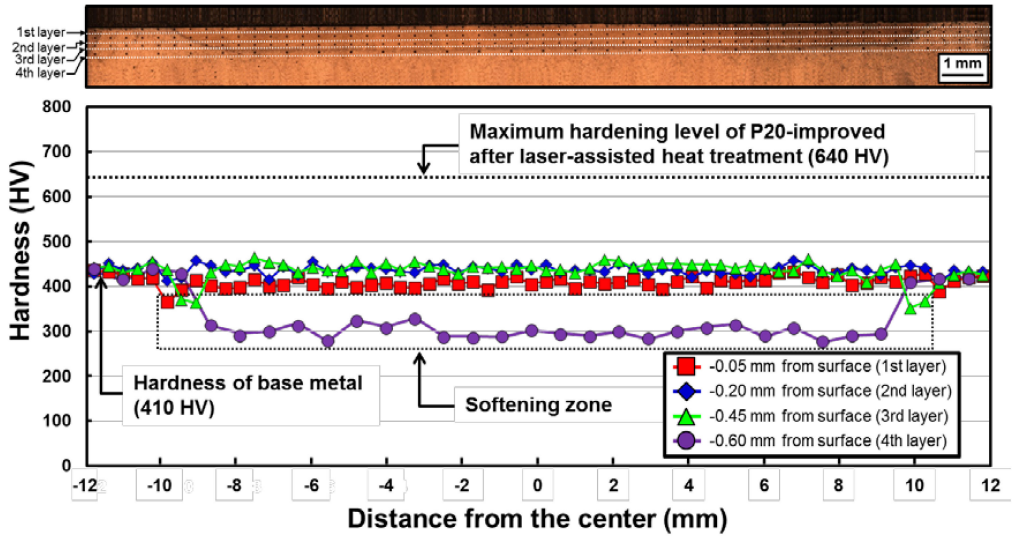

Figure 9. Hardness distribution and corresponding macrostructure of the heat-treated cross-sectional specimen at a temperature of 1473 K for P21 steel.

3.6. Microstructural Characterization of the Hardening Zone in P20-Improved Steel

Figure 10 shows typical SEM and scanning transmission electron microscopy (STEM) micrographs within the hardening zone of P20-improved after heat treatment at 1473 K. The observation area ("A", "B", and "C") is schematically described in Figure 10. The typical lath morphology of martensite was observed within the overall hardening zone. At other heat treatment temperatures, this type of martensite was clearly confirmed. Figure 11 depicts a representative TEM bright field (BF) and high-resolution (HR) images with the corresponding selected area electron diffraction (SAED) pattern and fast Fourier transform (FFT) pattern for P20-improved at a heat-treatment temperature of 1473 K. The observation area corresponds to position "B" in Figure 10. Martensite was characterized together with {112}<111> type twinning as a substructure. In other words, the reason for the hardness increase (i.e., formation of the hardening zone) after laser-assisted heat treatment of P20-improved could be martensite transformation hardening.

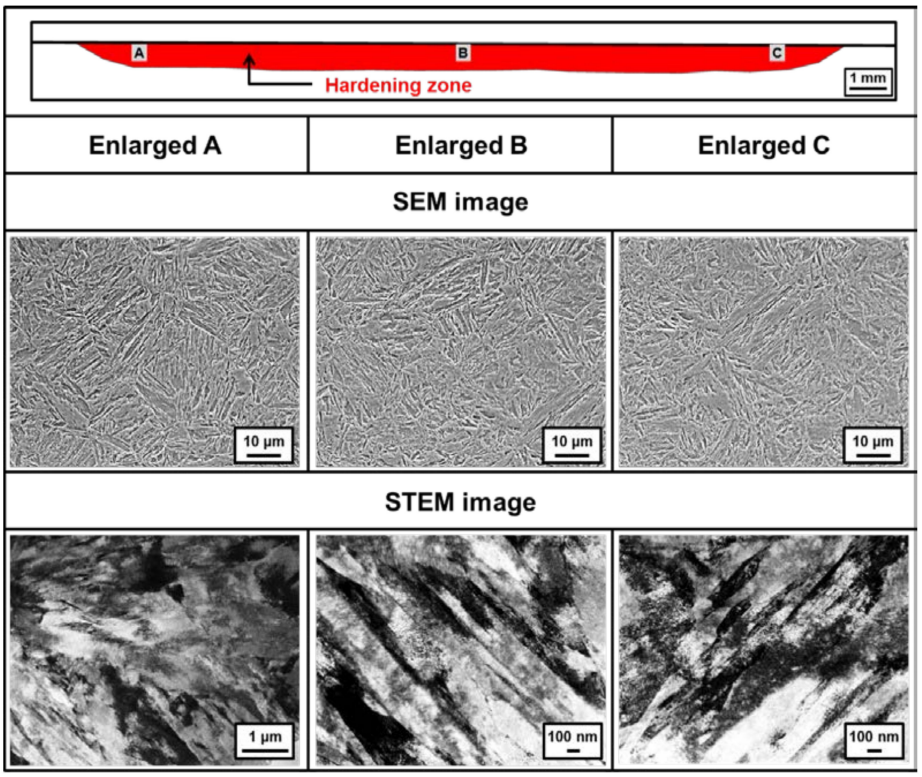

Figure 10. Typical SEM and STEM micrographs of the hardening zone of P20-improved steel after laser-assisted heat treatment at 1473 K.

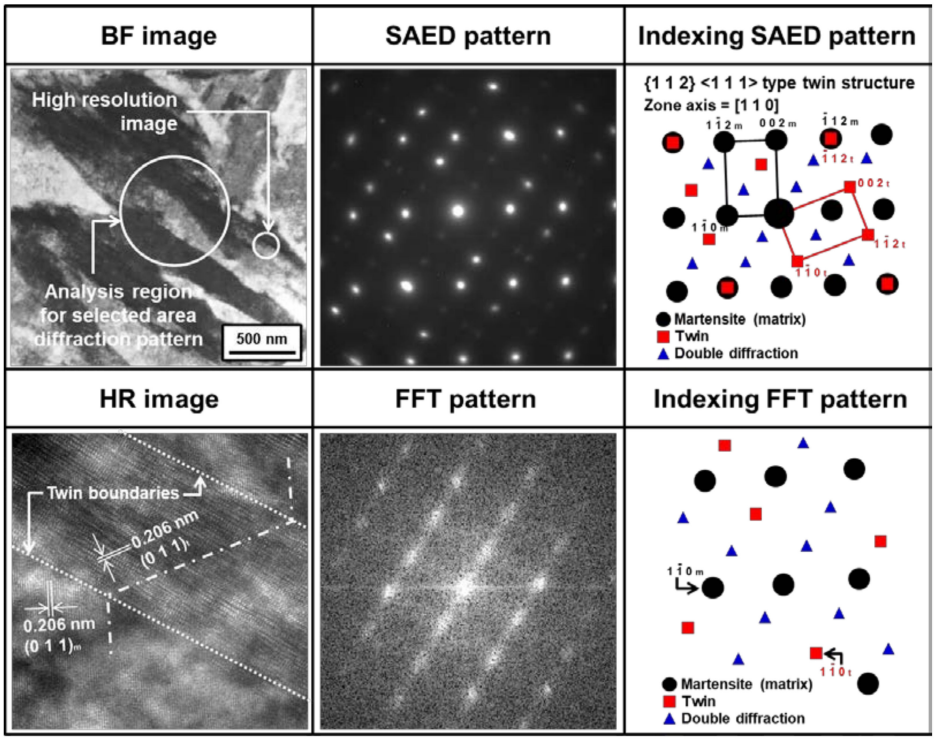

Figure 11. Representative BF and HR images of the hardening zone of P20-improved steel after laser-assisted heat treatment at 1473 K and its corresponding SAED and FFT patterns analyzed by TEM.

Figure 12 demonstrates SEM micrographs for the boundary region between the hardening zone and the base metal region for the same specimen described in Figure 10. The observation area ("C" and "D") is also schematically indicated in Figure 12. Although tempered martensite was mainly observed in this boundary region as similar to the microstructure of base metal, this microstructural distribution did not cause a further decrease of hardness level below the hardness of base metal, as described in Figure 8.

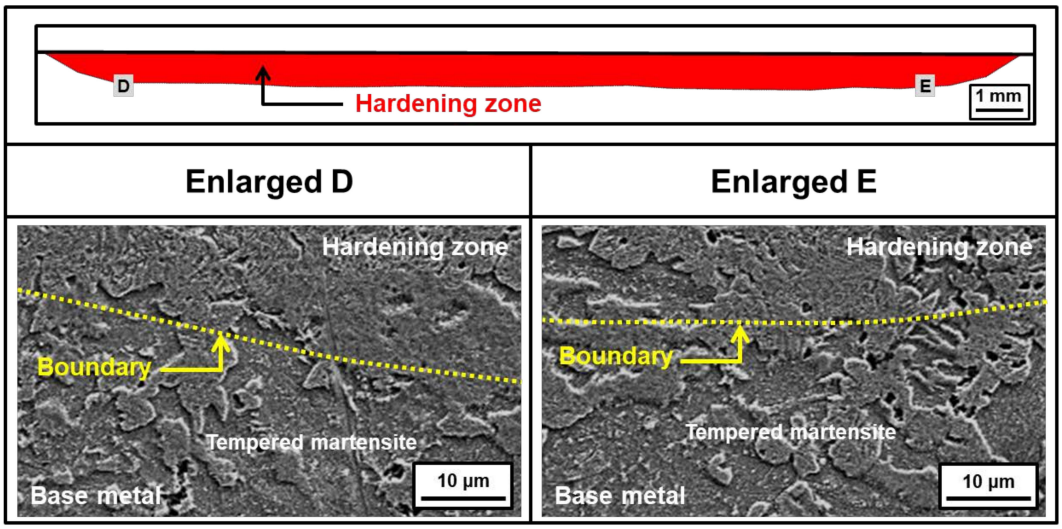

Figure 12. SEM micrographs of the boundary between the hardening zone and the base metal region of P20-improved steel after laser-assisted heat treatment at 1473 K.

3.7. Relationship between Coarsening of Cu Precipitates and Formation of the Softening Zone in P21 Steel

Figure 13 shows typical SEM and STEM images observed within the heat-treated zone for P21 at a heat treatment temperature of 1473 K. The observation area ("A" and "B") is schematically designated in Figure 13. Similar to P20-improved, the overall heat-treated zone consisted of a lath-type martensite phase. However, the hardness within the heat-treated zone (corresponding to regions "A" and "B" in Figure 13) was similar to that of the base metal, despite the accompanying martensite transformation for P21 steel as described in Figure 9. Thus, we clearly confirmed that the laser-assisted heat treatment process cannot always effectively improve the performance of surfaces such as P21 steel.

Figure 14 depicts representative SEM micrographs for the boundary region between the heat-treated zone and the base metal (indicated by "C") for P21 steel, which demonstrates softening phenomena after laser-assisted heat treatment, as mentioned in Figure 9. Figure 14 also shows SEM micrographs of the base metal region away from the heat-treated zone (indicated by "D"). The overall microstructure in the softening zone and the base metal region consisted of tempered martensite, and thickness of the softening zone was approximately 40 μm. For the softening zone (at region "C" in Figure 14), the reason for the formation of the tempered martensite was regarded as the heat cycle during the laser-assisted heat treatment. However, more enlarged views (SEM micrographs labeled "Enlarged C-1" and "Enlarged D-1" in Figure 14) show different microstructures between the softening zone and the base metal region; therefore, the microstructure of the base metal region indicates that fine particles were more densely distributed within the tempered martensite phase than in the softening zone. The particles were larger and more loosely distributed than in the base metal region. Consequently, the formation of the softening zone in P21 steel after laser-assisted heat treatment is discussed according to this particle distribution.

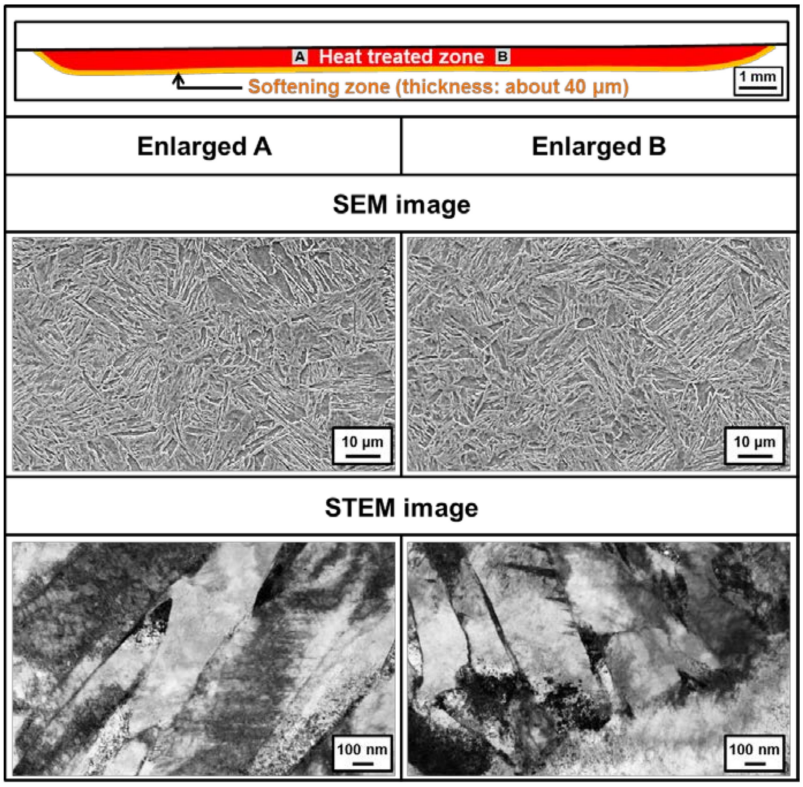

Figure 13. Typical SEM and STEM micrographs of the heat-treated zone of P21 steel after laser-assisted heat treatment at 1473 K.

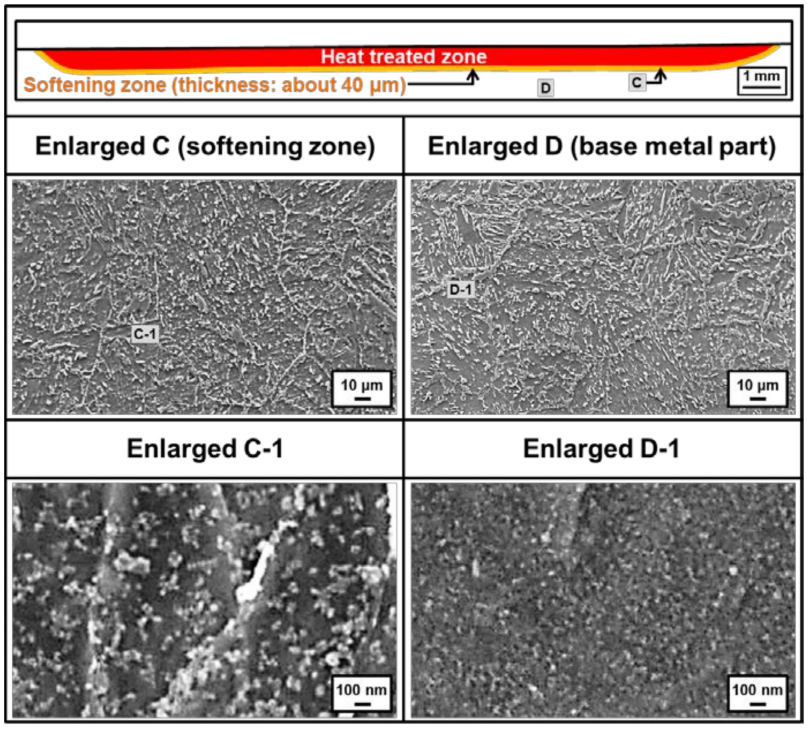

Figure 14. Comparison of SEM micrographs of the softening zone and base metal region of P21 steel after laser-assisted heat treatment at 1473 K.

Figure 15 shows TEM micrographs obtained by the replica method of the softening zone and base metal region. Even though the circular shape of precipitates was observed in both regions, their size differed, as confirmed by SEM images in Figure 14. Figure 16 also shows the representative element composition and SAED pattern of this precipitate. As a result, this circular precipitate was characterized as a Cu particle in both the softening zone and base metal region. Figure 17 shows the quantitative results of Cu precipitate size distribution measured from TEM analysis for both the softening zone (Figure 17a) and the base metal part (Figure 17b). This size distribution was summarized from ten BF images with dimensions of 5 × 5 μm. In the softening zone (in Figure 17a), approximately 80% of Cu precipitates have diameters from 101 nm to 270 nm. The largest diameter of Cu precipitates observed by TEM in this study was 263 nm. On the other hand, in the base metal region (in Figure 17b), the largest diameter of Cu precipitates was approximately 27 nm, and 87% of Cu precipitates were below 20 nm in diameter.

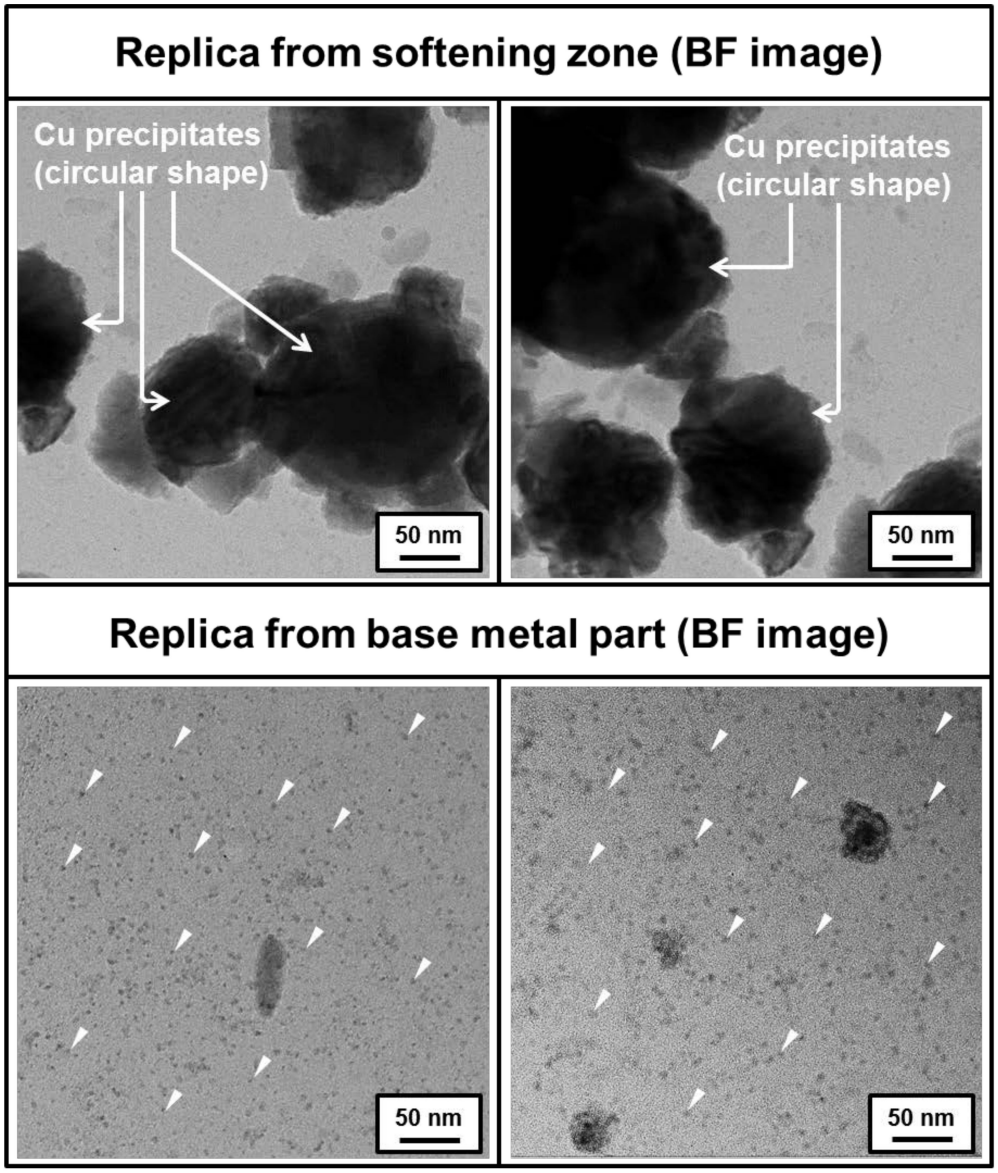

Figure 15. Comparison of TEM micrographs obtained from the replica method for the softening zone and the base metal region of P21 steel after laser-assisted heat treatment at 1473 K.

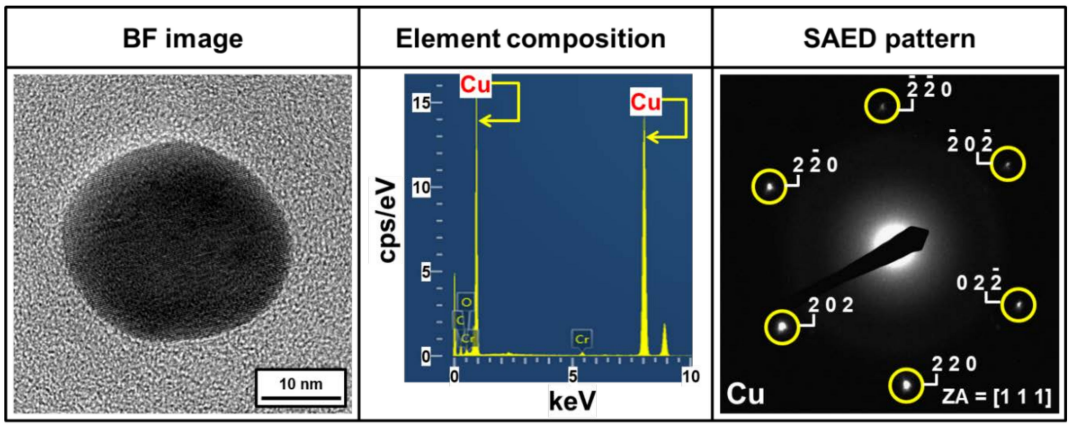

Figure 16. Representative TEM micrograph (Cu precipitates) obtained using the replica method for the base metal region of P21 steel after laser-assisted heat treatment at 1473 K and its corresponding EDS and SADP analysis.

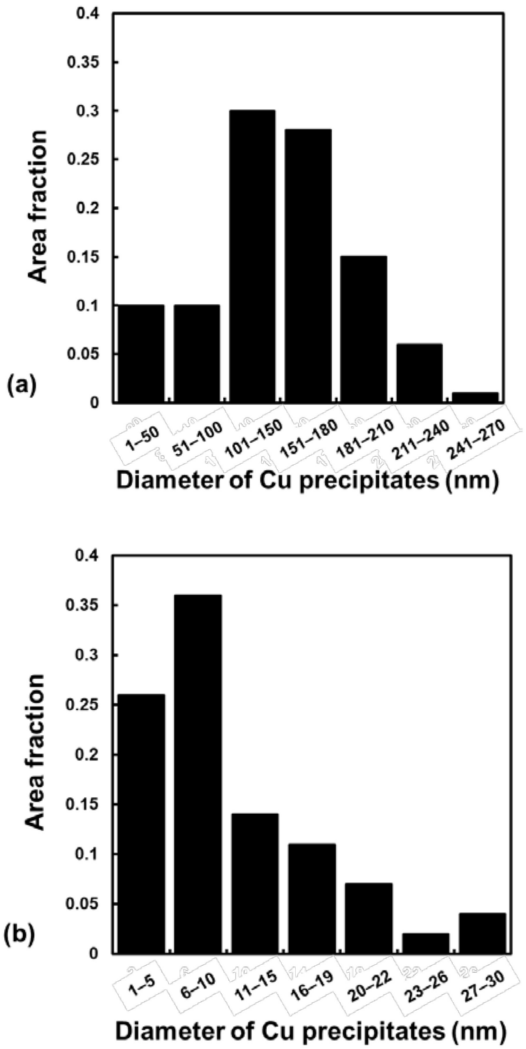

Figure 17. Size distribution of Cu precipitates of P21 steel after laser-assisted heat treatment at 1473 K: (**a**) softening zone and (**b**) base metal region.

Consequently, it follows that the reason for the appearance of a softening zone in P21 steel instead of a base metal region after laser-assisted heat treatment, as described in Figure 9, could be regarded as coarsening of Cu precipitates, despite possessing the same matrix phase (i.e., tempered martensite) for both the softening zone and base metal region. Furthermore, it can be speculated that this coarsening behavior in the softening zone is highly related to overaging during laser-assisted heat treatment.

4. Conclusions

In this study, laser-assisted surface heat treatment was performed to achieve superior mechanical performance for two types of plastic injection mold steel (P20-improved and P21) using a high-power diode laser with in situ control over the temperature and laser power. The following conclusions were drawn from this study.

For the experimental design of laser-assisted heat treatment, the temperature conditions were set within the austenite single-phase region, and the set temperatures were calculated using thermodynamic software and the compositions of P20-improved and P21 steels. For P20-improved, a hardness increase of 120% from the base metal level (290 HV) was achieved through heat treatment using a high-power diode laser at a temperature of 1473 K. Also, martensite transformation was regarded as the major hardening mechanism of the heat-treated P20-improved steel. However, for P21 steel, hardness values within the heat-treated zone did not change from that of the base metal (410 HV) after laser-assisted heat treatment (i.e., surface hardening was not achieved through the laser-assisted heat treatment process for P21 steel). Moreover, it was clearly observed that the hardness dropped below the base metal level at the boundary between the heat-treated zone and the base metal region, revealing the formation of a softening zone. Coarsening of Cu precipitates is proposed as the reason for the appearance of the softening zone in the heat-treated P21 steel, despite both the softening zone and the base metal region possessing the same matrix phase (i.e., tempered martensite).

Author Contributions: Conceptualization, E.-J.C.; Methodology, E.-J.C.; Software, E.-J.C.; Formal Analysis, A.S.; and M.-S.K.; Investigation, A.S.; Data Curation, E.-J.C.; Writing-Original Draft Preparation, E.-J.C.; Writing-Review & Editing, N.K. and E.-J.C.; Supervision, N.K.; Project Administration, E.-J.C.; Funding Acquisition, E.-J.C.

Funding: This research was funded by Ministry of SMEs and Startups, Republic of Korea grant number AI2870 and Korea Institute of Machinery and Materials, Republic of Korea grant number NK214T.

Acknowledgments: The authors would like to thank Department of Materials Science and Engineering, Pusan National University, Republic of Korea for help in sample preparation for microstructural analysis.

Conflicts of Interest: The authors declare no conflict of interest.

References

1. Shiou, F.J.; Cheng, C.H. Ultra-precision surface finish of NAK80 mould tool steel using sequential ball burnishing and ball polishing processes. *J. Mater. Process. Technol.* **2018**, *201*, 554–559. [CrossRef]
2. Singh, G.; Verma, A. A brief review on injection moulding manufacturing process. *Mater. Today-Proc.* **2017**, *4*, 1423–1433. [CrossRef]
3. Silva, F.J.G.; Martinho, R.P.; Alexandre, R.J.D.; Baptista, A.P.M. Increasing the wear resistance of molds for injection of glass fiber reinforced plastics. *Wear* **2011**, *271*, 2494–2499. [CrossRef]
4. Boztepe, E.; Alvesb, A.C.; Ariza, E.; Rocha, L.A.; Cansever, N.; Toptan, F. A comparative investigation of the corrosion and tribocorrosion behavior of nitrocarburized, gas nitrided, fluidized-bed nitrided, and plasma nitride plastic mould steel. *Surf. Coat. Technol.* **2018**, *334*, 116–123. [CrossRef]
5. Wen, D.C. Microstructure and corrosion resistance of the layers formed on the surface of precipitation hardenable plastic mold steel by plasma-nitriding. *Appl. Surf. Sci.* **2009**, *256*, 797–804. [CrossRef]
6. Chun, E.J.; Nishimoto, K.; Saida, K. Evaluation of solidification cracking susceptibility in laser welds for type 316FR stainless steel. *Weld. World* **2016**, *60*, 217–231. [CrossRef]
7. Chun, E.J.; Lee, S.J.; Suh, J.; Kang, N.; Saida, K. Solidification cracking behavior in austenitic stainless steel laser welds (part 1)—Evaluation of solidification cracking susceptibility by laser beam welding Varestraint test. *J. Weld. Join.* **2016**, *34*, 54–60. [CrossRef]

8. Chun, E.J.; Lee, S.J.; Suh, J.; Kang, N.; Saida, K. Solidification cracking behavior in austenitic stainless steel laser welds (part 2)—Effects of δ–ferrite crystallization and solidification segregation behavior on solidification cracking susceptibility. *J. Weld. Join.* **2016**, *34*, 61–69. [CrossRef]
9. Zhang, Z.; Yu, T.; Kovacevic, R. Erosion and corrosion resistance of laser cladded AISI 420 stainless steel reinforced with VC. *Appl. Surf. Sci.* **2017**, *410*, 225–240. [CrossRef]
10. Cong, D.; Zhou, H.; Ren, Z.; Zhang, H.; Ren, L.; Meng, C.; Wang, C. Thermal fatigue resistance of hot work die steel repaired by partial laser surface remelting and alloying process. *Opt. Lasers Eng.* **2014**, *54*, 55–61. [CrossRef]
11. Tong, X.; Dai, M.J.; Zhang, Z.H. Thermal fatigue resistance of H13 steel treated by selective laser surface melting and CrNi alloying. *Appl. Surf. Sci.* **2013**, *217*, 373–380. [CrossRef]
12. Sun, P.; Li, S.; Yu, G.; He, X.; Zheng, C.; Ning, W. Laser surface hardening of 42CrMo cast steel for obtaining a wide and uniform hardened layer by shaped beams. *Int. J. Adv. Manuf. Technol.* **2014**, *70*, 787–796. [CrossRef]
13. Wang, C.; Zhou, H.; Liang, N.; Wang, C.; Cong, D.; Meng, C.; Ren, L. Mechanical properties of several laser remelting processed steels with different unit spacings. *Appl. Surf. Sci.* **2014**, *313*, 333–340. [CrossRef]
14. Lee, K.H.; Choi, S.W.; Yoon, T.J.; Kang, C.Y. Microstructure and hardness of surface melting hardened zone of mold steel, SM45C using Yb:YAG disk laser. *J. Weld. Join.* **2016**, *34*, 75–81. [CrossRef]
15. Hongchao, Q. Experimental investigation of laser peening on Ti17 titanium alloy for rotor blade applications. *Appl. Surf. Sci.* **2015**, *351*, 524–530. [CrossRef]
16. Hoppius, J.S.; Kukreja, L.M.; Knyazeva, M.; Pohl, F.; Walther, F.; Ostendorf, A.; Gurevich, E.L. On femtosecond laser shock peening of stainless steel AISI 316. *Appl. Surf. Sci.* **2018**, *435*, 1120–1124. [CrossRef]
17. Haque, R. Quality of self-piercing riveting (SPR) joints from cross-sectional perspective: A review. *Arch. Civ. Mech. Eng.* **2018**, *18*, 83–93. [CrossRef]
18. Chun, E.J.; Kim, M.S.; Nishikawa, H.; Park, C.; Suh, J. Laser-assisted selective fusing of thermal sprayed Ni-based self-fluxing alloys by using high–power diode lasers. *Opt. Lasers Technol.* **2018**, *100*, 317–324. [CrossRef]
19. Syed, B.; Shariff, S.M.; Padmanabham, G.; Lenka, S.; Bhattacharya, B.; Kundu, S. Influence of laser surface hardened layer on mechanical properties of re-engineered low carbon steel sheet. *Mat. Sci. Eng. A* **2017**, *685*, 168–177. [CrossRef]
20. Guarino, S.; Barletta, M.; Afilal, A. High power diode laser (HPDL) surface hardening of low carbon steel: Fatigue life improvement analysis. *J. Manuf. Process.* **2017**, *28*, 266–271. [CrossRef]
21. Telasang, G.; Majumdar, J.D.; Padmanabham, G.; Manna, I. Wear and corrosion behavior of laser surface engineered AISI H13 hot working tool steel. *Surf. Coat. Technol.* **2015**, *261*, 69–78. [CrossRef]
22. Telasang, G.; Majumdar, J.D.; Padmanabham, G.; Manna, I. Structure-property correlation in laser surface treated AISI H13 tool steel for improved mechanical properties. *Mat. Sci. Eng. A* **2014**, *599*, 255–267. [CrossRef]
23. Shariff, S.M.; Pal, T.K.; Padmanabham, G.; Joshi, S.V. Influence of chemical composition and prior microstructure on diode laser hardening of railroad steels. *Surf. Coat. Technol.* **2013**, *228*, 14–26. [CrossRef]
24. Santhanakrishnan, S.; Kovacevic, R. Hardness prediction in multi-pass direct diode laser heat treatment by on-line surface temperature monitoring. *J. Mater. Process. Technol.* **2012**, *212*, 2261–2271. [CrossRef]
25. Li, R.; Jin, Y.; Li, Z.; Qi, K. A Comparative study of high-power diode laser and CO_2 laser surface hardening of AISI 1045 steel. *J. Mater. Eng. Perform.* **2014**, *23*, 3085–3091. [CrossRef]
26. Soriano, C.; Leunda, J.; Lambarri, J.; Navas, V.G.; Sanz, C. Effect of laser surface hardening on the microstructure, hardness and residual stressed of austempered ductile iron grades. *Appl. Surf. Sci.* **2011**, *257*, 7101–7106. [CrossRef]
27. Järvenpää, A.; Jaskari, M.; Hietala, M.; Mäntyjärvi, K. Local laser heat treatments of steel sheets. *Phys. Proc.* **2015**, *78*, 296–304. [CrossRef]
28. Qiu, F.; Uusitalo, J.; Kujanpaa, V. Laser transformation hardening of carbon steel: Microhardness analysis on microstructural phases. *Surf. Eng.* **2013**, *29*, 34–40. [CrossRef]
29. Farshidianfar, M.H.; Khajepouhor, A.; Gerlich, A. Real time monitoring and prediction of martensite formation and hardening depth during laser heat treatment. *Surf. Coat. Technol.* **2017**, *315*, 326–334. [CrossRef]

30. Hsiao, C.N.; Yang, J.R. Age hardening in martensitic/bainitic matrices in a copper-bearing steel. *Mater. Trans.* **2000**, *41*, 1312–1321. [CrossRef]
31. Jung, J.G.; Jung, M.; Kang, S.; Lee, Y.K. Precipitation behaviors of carbides and Cu during continuous heating for tempering in Cu-bearing medium C martensitic steel. *J. Mater. Sci.* **2014**, *49*, 2204–2212. [CrossRef]
32. Yao, C.; Xu, B.; Huang, J.; Zhang, P.; Wu, Y. Study on the softening in overlapping zone by laser-overlapping scanning surface hardening for carbon and alloyed steel. *Opt. Laser Eng.* **2010**, *48*, 20–26. [CrossRef]
33. Bouquet, J.; Camp, D.V.; Malek, O.; Haaf, P.T.; Vanmeensel, K.; Lauwers, B. Aiming for improved lifetime of die and mold components through an integrated laser hardening operation, combining machining and a selective heat treatment in one setup. *Proc. CIRP* **2016**, *46*, 541–544. [CrossRef]
34. Kwok, C.T.; Leong, K.I.; Cheng, F.T.; Man, H.C. Microstructural and corrosion characteristics of laser surface-melted plastics mold steels. *Mater. Sci. Eng. A* **2003**, *357*, 93–103. [CrossRef]